

# Consequences of melt transport for uranium series disequilibrium in young lavas

Marc Spiegelman and Tim Elliott  
Lamont-Doherty Earth Observatory  
of Columbia University

Earth Planet. Sci. Letts.  
118 (1993) 1–20

## Abstract

Radioactive disequilibrium of  $^{238}\text{U}$  nuclides is commonly observed in young lavas and has often been used to infer the rates of melting and melt migration. However, previous calculations do not actually include melt transport. Here we explore the behaviour of short-lived radionuclides in a new calculation that includes the fluid dynamics of melt segregation. We emphasize that  $^{238}\text{U}$  series disequilibrium results from the differences in residence time of parent and daughter nuclides. Unlike previous models, contrasts in residence times are controlled by differences in transport velocities caused by melt separation and continued melt-solid interaction throughout the melting column. This “chromatographic” effect can produce larger excesses of both  $^{230}\text{Th}$  and  $^{226}\text{Ra}$  within the same physical regime compared to previous calculations which do not include melt transport. Using this effect to account for U-series excesses leads to radically different inferences about the rates of melt migration. Where previous models require rapid melt extraction, our calculation can produce larger excesses with slow melt extraction. Nevertheless, reproducing the large  $(^{226}\text{Ra}/^{230}\text{Th})$  activity ratios observed in fresh mid-ocean ridge glasses is still problematic if the residence times are controlled solely by bulk equilibrium partitioning. While it still remains to be shown conclusively that the large  $^{226}\text{Ra}$  excesses are produced during melting, our calculation only requires differences in transport velocities to produce secular disequilibrium. Thus we speculate that other processes, such as crystal surface interaction, may also contribute to the production of the observed excesses.

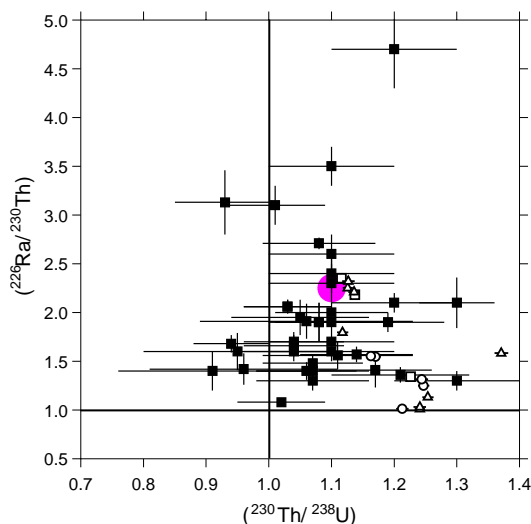


Figure 1: Activity ratios of  $(^{230}\text{Th}/^{238}\text{U})$  and  $(^{226}\text{Ra}/^{230}\text{Th})$  for axial mid-ocean ridge basalts from the East Pacific Rise (squares), Juan de Fuca Ridge (triangles) and Gorda Ridge (circles). Measurements are made using alpha counting [3-5] (solid symbols) and mass spectrometry [6] (open symbols) and are shown with  $2\sigma$  error bars. The activity ratio of any two elements is the ratio of their decay rates e.g.  $(^{230}\text{Th}/^{238}\text{U}) = \lambda_{Th}[^{230}\text{Th}]/\lambda_U[^{238}\text{U}]$  where square brackets denote atomic concentrations and  $\lambda$  is the decay constant. In general, young mid-ocean ridge basalts show excesses of both  $^{230}\text{Th}$  and  $^{226}\text{Ra}$  with little apparent correlation between the two activity ratios. The grey circle marks the reference activity ratios of  $(^{230}\text{Th}/^{238}\text{U})= 1.1$  and  $(^{226}\text{Ra}/^{230}\text{Th})= 2.25$  that appear in subsequent contour plots.

## 1 Introduction

$^{238}\text{U}$  decays to stable  $^{206}\text{Pb}$  via a chain of short-lived intermediate nuclides which includes  $^{230}\text{Th}$  and

$^{226}\text{Ra}$ . In a closed system, such a decay series evolves to a state of secular equilibrium where the decay rate (activity) of each intermediate nuclide equals its production rate due to the decay of its respective parent element. Therefore, in secular equilibrium the ratio of activities of any two nuclides in the chain are unity. If such a system is disturbed, excesses (activity ratios  $> 1$ ) will relax towards unity on a time scale that is of the order of the half-life of the daughter nuclide. The half-lives of  $^{230}\text{Th}$  and  $^{226}\text{Ra}$  are 75,380 yr and 1600 yr respectively, which makes them particularly useful for investigating melting and melt migration processes. Moreover, these nuclides are short-lived relative to time-scales of mantle evolution so that a mantle source is very likely to be in secular equilibrium before melting commences. Thus, unlike most geochemical systems, the  $^{238}\text{U}$  series nuclides have a well constrained source composition and provide information about the rates of geophysical processes.

Secular disequilibrium is commonly observed in fresh lavas from mid-ocean ridges, arcs and ocean-islands (see [1, 2] for reviews). Here we discuss a range of processes that can occur in all magmatic settings; however, we will focus principally on  $^{238}\text{U}$  series data from mid-ocean ridge basalts because the physical parameters controlling melting beneath ridges are best constrained. Figure 1 shows the available data for samples of axial ridge basalts where full U-Th-Ra isotope systematics have been measured by either alpha counting [3-5] or by mass spectrometry [6]. While the data show considerable scatter, all points show both  $^{230}\text{Th}$  and  $^{226}\text{Ra}$  excesses (within error). The principal problems posed by these observations is how to explain the apparent fractionations of very incompatible elements in large degree melts and how to preserve large  $^{226}\text{Ra}$  excesses given its short half-life of 1600 years.

This paper explores a range of processes that can cause secular disequilibrium in young lavas. Previous calculations have suggested that  $^{230}\text{Th}$  excesses can be produced by slow equilibrium melting and instantaneous melt extraction [7, 8]. Other models have invoked rapid disequilibrium melting [9]. While these previous calculations have been used to infer the rates of melting and melt extraction, it is important to note that none of these models actually include the fluid dynamics of melting and transport. The principal purpose of this paper is to illustrate how melt transport affects the behaviour of radiogenic nuclides and can lead

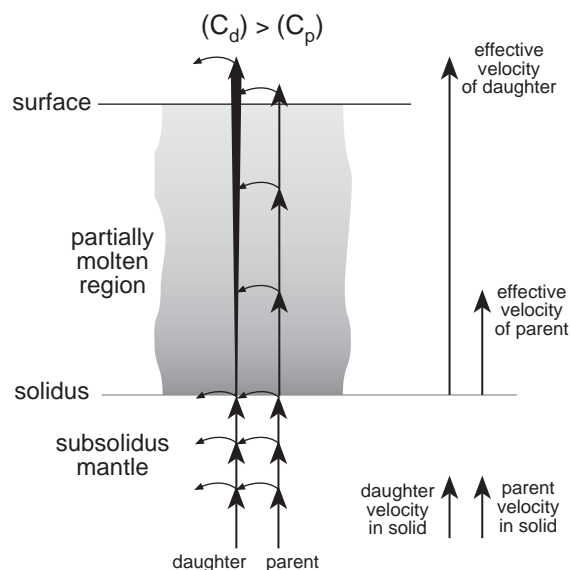


Figure 2: A schematic diagram to illustrate the effect of melt transport with continuous melt-solid interaction on parent and daughter activities,  $(c_p)$  and  $(c_d)$ , in a steady-state, one-dimensional melting column. The important property of this calculation is that different elements can travel at different velocities due to the “chromatographic effect” (e.g. [10, 11]) and therefore have different residence times in the column. The vertical arrows show the distance each element travels before a fixed percentage decays. The short curved arrows denote this decay. In the unmelted region below the solidus, both parent and daughter travel at the same velocity and can maintain secular equilibrium by decaying at the same rate. In the melting column, however, the daughter is less compatible and travels faster than the parent. In this case, the original daughter nuclides that enter the bottom can be extracted before they decay. This initial daughter, however, will be augmented by the decay of its parent, which spends more time in the column. This process is indicated by the increasing width of the daughter arrow. Thus the total concentration of the daughter at the surface will be enriched relative to the concentration at the base (here by a factor of  $\sim 3$ ).

to significantly different interpretations of the data.

## 2 Description of the model

The specific model we consider, calculates the melting, transport and decay of a series of elements ( $^{238}\text{U} \xrightarrow{2\alpha+2\beta} ^{230}\text{Th} \xrightarrow{\alpha} ^{226}\text{Ra}$ ) in a one-dimensional, steady-state upwelling column where we explicitly

calculate the flow of melt and solid. The model and its behaviour are shown schematically in Fig. 2. The elements are assumed to be in secular equilibrium when they begin melting. If all the elements continued to travel together as a closed system, they would decay at the same rate and remain in secular equilibrium. However, once the nuclides enter the partially molten region, they travel at different velocities due to the ‘‘chromatographic effect’’ described by many authors (e.g. [10, 11]). Because of their different transport velocities, each element has a different residence time in the melting column. If the parent spends more time in the column than the daughter, it will have more time to decay and thus will produce an excess of daughter nuclide. Here we develop the simplest quantitative description of this conceptual model to illustrate the fundamental effects of transport.

We begin with the general equation governing conservation of mass for each parent-daughter pair in a decay series of radioactive elements

$$\frac{\partial}{\partial t} [\rho_f \phi + \rho_s (1 - \phi) D_i] c_i^f + \nabla \cdot [\rho_f \phi \mathbf{v} + \rho_s (1 - \phi) D_i \mathbf{V}] c_i^f - \lambda_i [\rho_f \phi + \rho_s (1 - \phi) D_i] c_i^f = \lambda_{i-1} [\rho_f \phi + \rho_s (1 - \phi) D_{i-1}] c_{i-1}^f - \lambda_i [\rho_f \phi + \rho_s (1 - \phi) D_i] c_i^f \quad (5)$$

Here  $\rho_f$ ,  $\rho_s$  are the densities of the melt and solid respectively,  $\phi$  is the volume fraction of melt (porosity),  $\mathbf{v}$  is the melt velocity and  $\mathbf{V}$  is the solid velocity. For each element  $i = 1, 2, 3 \dots$  in the decay series,  $D_i$  is its bulk partition coefficient,  $c_i^f$  is its concentration in the melt and  $\lambda_i$  is its decay constant. Additional parameters and notation are given in Table 1. The first nuclide in the decay chain,  $^{238}\text{U}$ , has no parent and therefore  $\lambda_0 = 0$ . For simplicity, Eq. (1) neglects diffusion, and assumes that the concentration of element  $i$  in the melt and in the solid can always be related by a bulk partition coefficient  $D_i$ . Equation (1) states that changes in the total mass of element  $i$  depend on variations in the fluxes of melt and solid and on the balance of production by its parent (element  $i - 1$ ) and its own decay.

Of the principal unknowns in Eq. (1), the porosity and the melt and solid velocities are readily calculated given a mass-conservative theory of magma migration [12-17]. Appendix A shows that for a one-dimensional, steady-state melting column, the flux of melt and solid as a function of height,  $z$ , in the column can be written

$$\begin{aligned} \rho_f \phi w &= \Gamma_0 z & (2) \\ \rho_s (1 - \phi) W &= \rho_s W_0 - \Gamma_0 z & (3) \end{aligned}$$

where  $w$  is the one-dimensional melt velocity and  $W$  is the solid velocity (see also [18]). The term

$$\Gamma_0 = \frac{\rho_s W_0 F_{max}}{d} \quad (4)$$

is the constant melting rate in the column. Equation (4) approximates melting by adiabatic decompression by setting the melting rate proportional to the mantle upwelling rate,  $W_0$ .  $F_{max}$  is the maximum degree of melting attained at the top of the column (i.e. at height  $z = d$ ). Here the melting rate is constant, but these equations can be readily extended to include variable melting rates (see Appendix A).

Equations (2) and (3) show that the melt and solid fluxes simply balance melt production and vary linearly with height in the column. In particular, Eq. (2) shows that the melt flux increases with  $z$  but at any height, the product of porosity and melt velocity is fixed. If we note that  $F = F_{max} z / d$  is the degree of melting at height  $z$ , then Eqs. (2) and (4) can be combined to show that the relationship between melt velocity and porosity in steady state is

If the melt does not separate from the solid ( $w \rightarrow W_0$ ) then the porosity will be comparable to the degree of melting ( $\phi \sim F$ ). Very efficient melt extraction ( $w \gg W_0$ ) implies that the residual porosity must be very small and  $\phi \ll F$ . Once  $F(z)/\phi(z)$  is known at any height, the melt velocity is determined.

To determine  $\phi(z)$  requires an additional functional relationship between porosity and melt and solid velocities. Here we use a simplified form of Darcy’s law

$$\phi(w - W) = \frac{k_0}{\mu} \phi^n (1 - \phi) \Delta \rho g \quad (6)$$

to govern the separation of melt from solid.  $k_0$  controls the permeability and depends upon the spacing of melt channels [19],  $\mu$  is the melt viscosity and  $n$  is the power law exponent in the permeability that reflects the microscopic geometry of the melt distribution. If the melt is distributed in tubes  $n \sim 2$ . If it is in veins or sheets  $n \sim 3$  (e.g. [20]). Throughout this paper we use  $n = 2$ , although calculations using  $n = 3$  produce nearly identical results. Given Eqs. (2),(3) and (6) the porosity as a function of height is given implicitly by

$$\frac{\rho_f}{\rho} [\phi + A \phi^n (1 - \phi)^2] = \frac{F_{max} z}{d} \quad (7)$$

Table 1: Notation

Variable	Meaning	Values used	Dimension
$c_i^f$	concentration of component $i$ in melt		$\text{mol kg}^{-1}$
$c_{i0}^f$	initial concentration of component $i$ in melt ( $= c_{i0}^s/D_i$ )		$\text{mol kg}^{-1}$
$c_i^f$	$= c_i^f/c_{i0}^f$ dimensionless melt concentration		none
$c_{B_i}^f$	dimensionless melt concentration for a stable element		none
$c_i^s$	concentration of component $i$ in solid		$\text{mol kg}^{-1}$
$d$	depth to the solidus		m
$D_i$	bulk partition coefficient of element $i$		none
$\mathcal{D}_i^s$	diffusivity of element $i$ in solid	$(10^{-14}\text{--}10^{-18})$	$\text{m}^2 \text{s}^{-1}$
$\mathcal{D}_i^f$	diffusivity of element $i$ in melt	$(10^{-10}\text{--}10^{-11})$	$\text{m}^2 \text{s}^{-1}$
$F$	$= F(z) = F_{max}\zeta$ , degree of melting at height $z$	0–0.25	none
$F_{max}$	maximum degree of melting at top of column	0.25	none
$g$	acceleration due to gravity	9.81	$\text{m s}^{-2}$
$k_\phi$	permeability $= k_0\phi^n$		$\text{m}^2$
$k_0$	permeability constant		$\text{m}^2$
$n$	exponent in permeability	2	none
$t$	time		s
$t_{1/2}$	half-life		s
$t_c$	critical extraction time $= 6.64t_{1/2}$		s
$U_i$	$= \ln c_i^f$		none
$\mathbf{V}$	matrix velocity		$\text{m s}^{-1}$
$\mathbf{v}$	melt velocity		$\text{m s}^{-1}$
$W$	one-dimensional matrix velocity		$\text{m s}^{-1}$
$w$	one-dimensional melt velocity		$\text{m s}^{-1}$
$W_0$	initial solid upwelling rate	$10^{-3}\text{--}1$	$\text{m yr}^{-1}$
$w_{eff}^i$	effective velocity of component $i$		$\text{m s}^{-1}$
$z$	vertical cartesian coordinate (height)		m
$\alpha_i$	$= c_i^f/c_{B_i}^f$ enrichment factor over batch melting		none
$\Gamma$	melting rate		$\text{kg m}^{-3} \text{s}^{-1}$
$\Gamma_0$	constant melting rate		$\text{kg m}^{-3} \text{s}^{-1}$
$\zeta$	$= z/d$ dimensionless height in the column		none
$\lambda_i$	decay constant of element $i$		$\text{s}^{-1}$
$\mu$	melt shear viscosity	(1–10)	Pa s
$\rho_f$	density of melt	2800	$\text{kg m}^{-3}$
$\rho_s$	density of matrix	3300	$\text{kg m}^{-3}$
$\Delta\rho$	$= \rho_s - \rho_f$	500	$\text{kg m}^{-3}$
$\bar{\rho}$	$= \rho_f\phi + \rho_s(1 - \phi)$ mean density		$\text{kg m}^{-3}$
$\bar{\rho}_0$	mean density at porosity $\phi_{max}$		$\text{kg m}^{-3}$
$\phi$	porosity		none
$\phi_{max}$	maximum porosity in column	0.001–0.25	none
$\phi_{eq}$	equilibration volume (porosity) for dynamic melting	0–0.25	none

where

$$A = \frac{1}{\phi_{max}^{n-1}(1 - \phi_{max})^2} \left[ \frac{\bar{\rho}_0 F_{max}}{\rho_f \phi_{max}} - 1 \right] \quad (8)$$

and  $\phi_{max}$  is the maximum porosity at the top of the column. By combining Darcy's law with general mass conservation, we need only choose  $\phi_{max}$  and  $F_{max}$  to determine the porosity and melt and solid velocities throughout the column. (see also [18, 21])

Equation (1) can now be rewritten in a more tractable form using Eqs. (2), (3) and (7). For simplicity we use constant bulk partition coefficients and assume that the solid is initially in secular equilibrium before melting begins. This initial condition is

$$\frac{\lambda_i c_{i0}^f D_i}{\lambda_{i-1} c_{(i-1)0}^f D_{i-1}} = 1 \quad (9)$$

We scale the concentrations of each element in the melt to the initial *melt* concentrations (i.e.  $c_i^f = c_i^f / c_{i0}^f$ ), and scale the distance to the depth of the melting column. With these considerations Eq. (1) becomes

$$\frac{dc_i^f}{d\zeta} = c_i^f \frac{(D_i - 1)F_{max}}{D_i + (1 - D_i)F_{max}\zeta} + \lambda_i d \left[ B(\zeta) \frac{c_{i-1}^f}{w_{eff}^{i-1}} - \frac{c_i^f}{w_{eff}^i} \right]$$

where

$$B(\zeta) = \frac{D_i [D_{i-1} + (1 - D_{i-1})F_{max}\zeta]}{D_{i-1} [D_i + (1 - D_i)F_{max}\zeta]} \quad (11)$$

and  $\zeta = z/d$  is the fractional height in the column (i.e.  $\zeta = 0$  at the base of the column and  $\zeta = 1$  at the top). Equation (10) forms a system of ordinary differential equations that can be solved for the concentrations of each element in the decay series using standard numerical techniques [22]. The first term on the right hand side is the change in concentration due to melting. The second term is the change in concentration due to the difference between production and decay of the daughter element. The radiogenic production term depends primarily on the ‘‘effective velocity’’ of each element  $i$  (e.g. [10, 11])

$$w_{eff}^i = \frac{\rho_f \phi w + \rho_s (1 - \phi) D_i W}{\rho_f \phi + \rho_s (1 - \phi) D_i} = W_0 \frac{D_i + (1 - D_i) \frac{\rho_f \phi}{\rho_s (1 - \phi)}}{D_i + (\rho_f / \rho_s - D_i) \phi} \approx W + \frac{1}{1 + D_i / \phi} (w - W)$$

which is a weighted combination of the melt and solid velocities. Elements with partition coefficients greater

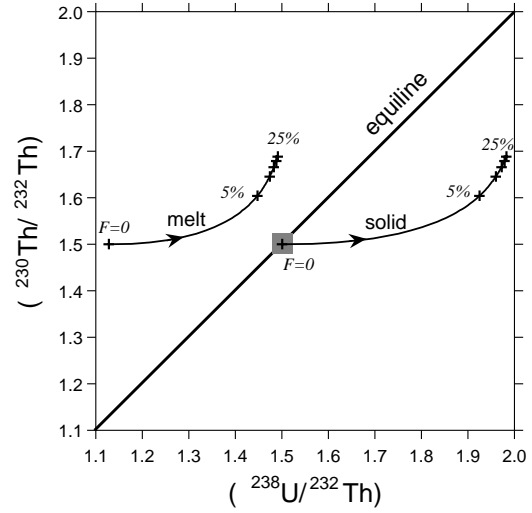


Figure 4: Activities of  $^{238}\text{U}$  and  $^{230}\text{Th}$  in both the solid and the melt from Fig. 3b plotted on a conventional equiline diagram. The trajectories show the changes in activity as a function of height in the column.  $F = 0$  is the bottom of the column,  $F = 0.25$  is the top. The activity ratio in the initial solid lies on the equiline while  $(^{230}\text{Th}/^{238}\text{U})$  in the first liquid is the ratio of parent to daughter bulk partition coefficients (here  $D_U/D_{Th} = 1.33$ ). As the degree of melting increases up the column, elemental fractionation of U and Th becomes insignificant and so the  $(^{238}\text{U}/^{232}\text{Th})$  ratio of the melt rapidly approaches that of the initial solid (grey square). The  $(^{230}\text{Th}/^{232}\text{Th})$  ratio, however, increases in both melt and solid as  $^{238}\text{U}$  decays to produce  $^{230}\text{Th}$ . This ‘‘ingrowth’’ of  $^{230}\text{Th}$  is evident in the equiline diagram. The corresponding decay of  $^{238}\text{U}$  is not apparent only because atomic concentrations of  $^{238}\text{U}$  are always over 4 orders of magnitude greater than those of  $^{230}\text{Th}$  (e.g. in secular equilibrium  $[^{238}\text{U}/^{230}\text{Th}] = \lambda_{Th}/\lambda_U = 5.9 \times 10^4$ ). Thus the number of decays of  $^{238}\text{U}$  over melting time scales has negligible effects on uranium concentrations but large effects on  $^{230}\text{Th}$  abundances. The process of ingrowth of  $^{230}\text{Th}$  is the same as that demonstrated in [7, 8] but here is controlled by transport processes rather than melting processes (see Section 4).

than the porosity ( $D_i \gg \phi$ ) travel near the solid velocity. Very incompatible elements ( $D_i \ll \phi$ ) travel near the melt velocity. Thus, as long as melt separates from the solid, elements with different solid/liquid partitioning will travel at different velocities. While Eq. (10) appears somewhat complicated, this calculation has fewer free parameters than previous models because it provides the important coupling between melting, porosity, and the velocity of each element.

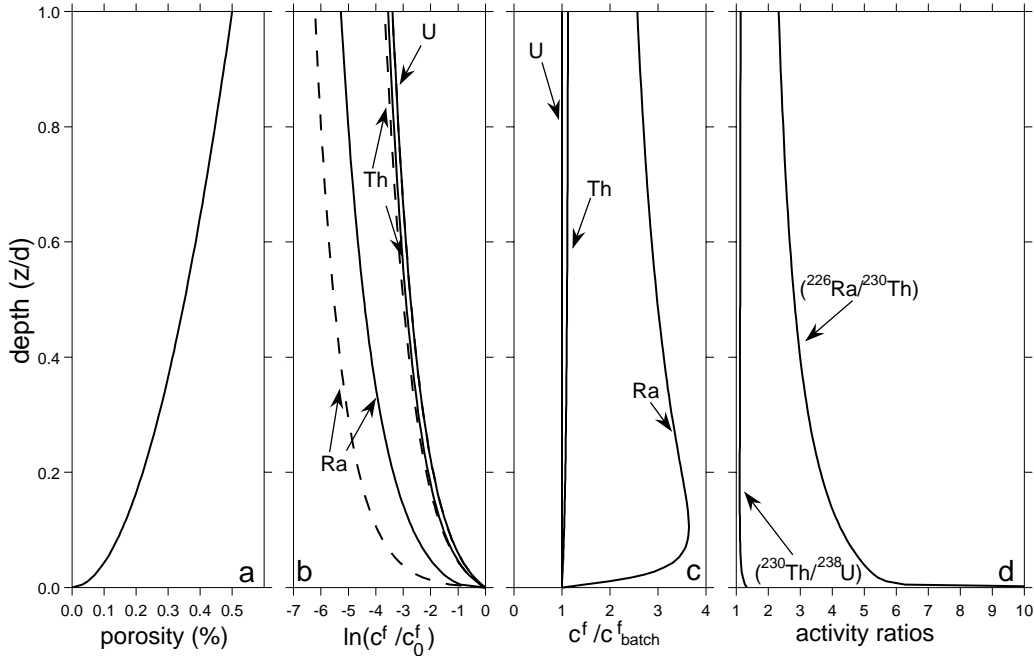


Figure 3: Solutions for porosity, concentrations of  $^{238}\text{U}$ ,  $^{230}\text{Th}$ ,  $^{226}\text{Ra}$  and activity ratios ( $^{230}\text{Th}/^{238}\text{U}$ ), ( $^{226}\text{Ra}/^{230}\text{Th}$ ) as a function of height in the melting column ( $d = 50\text{km}$ ). In this particular solution, the maximum porosity is  $\phi_{max} = 0.005$ , the upwelling velocity is  $W_0 = 0.05 \text{ m yr}^{-1}$  and the maximum degree of melting at  $z = d$  is  $F_{max} = 0.25$ . The effective bulk partition coefficients used are  $D_U = 0.0086$ ,  $D_{Th} = 0.0065$  and  $D_{Ra} = 0.0005$ . (a) Profile of porosity with depth. (b) Concentrations of  $^{238}\text{U}$ ,  $^{230}\text{Th}$  and  $^{226}\text{Ra}$  with depth. The solid lines show the natural log of the melt concentration normalized to the initial melt concentration  $c_0^f/D$ . The dashed lines show the concentrations expected if there was no radioactive decay (which is the same as expected with batch melting). (c) The excess concentration of each element with respect to batch melting,  $\alpha_i$  (see Eq. 14). Each curve shows the ratio of the element concentration to the concentration of a stable element with the same partition coefficient (e.g. the curve marked Th is the  $^{230}\text{Th}/^{232}\text{Th}$  ratio normalized to its source ratio). The enrichments in both  $^{230}\text{Th}$  and  $^{226}\text{Ra}$  arise from the decay of the parent element that is preferentially retained in the column. (d) Activity ratios as a function of depth. In this instance,  $(^{230}\text{Th}/^{238}\text{U}) = 1.13$  and  $(^{226}\text{Ra}/^{230}\text{Th}) = 2.3$  at the surface.

### 3 Behaviour of the system

This section describes the behaviour of Eq. (10) to illustrate the consequences of melt transport in the simplest system. Figure 3 shows one solution of these equations for a set of parameters that can produce  $^{230}\text{Th}$  and  $^{226}\text{Ra}$  excesses comparable to the reference values in Fig. 1. This figure (and Fig. 5), however, should not be taken as a model for MORB. In particular, a number of partitioning experiments suggest that the assumption of a single set of constant bulk partition coefficients inherent in Eq. (10) is inadequate to describe MORB genesis [23-28]. Nevertheless, all of the important effects of melt transport are contained in the simplest calculation and more realistic sets of parameters can be added without changing the basic nature of the solution (see Discussion and Appendix).

Furthermore, previous calculations have also assumed single stage melting and the results of all of the models can be readily compared for the same parameters. After we discuss the range of processes that can affect U-series disequilibrium we will consider additional models that are more relevant for MORB genesis.

Figure 3a shows the porosity as a function of height in a melting column of depth  $d = 50\text{km}$  where the mantle upwells at  $W_0 = 5 \text{ cm yr}^{-1}$ . In this calculation, the solid undergoes 25% melting by the time it reaches the top of the column. The maximum porosity, however, is only 0.5% and thus the melt moves approximately 50 times faster than the solid (Eq. 5) and takes  $\sim 20,000 \text{ yrs}$  to traverse the melting column. Figure 3b shows the natural log of the concentration normalized to the concentration of the initial liquid ( $U_i = \ln[c_i^f/c_{i0}^f]$ ) for  $^{238}\text{U}$ ,  $^{230}\text{Th}$ , and  $^{226}\text{Ra}$ . For

comparison, the dashed lines show the concentrations expected if the elements were non-radiogenic (i.e. if  $\lambda_i = 0$  for all elements). Inspection of Eq. (10) shows that if changes in concentration are due only to melting, then the concentration of each element in the melt would be

$$c'_i = \frac{D_i}{D_i + (1 - D_i)F_{max}\zeta} \quad (13)$$

which is identical to the concentrations expected in *batch* melting even though the porosity is small and the melt moves relative to the solid. This result has been noted before (e.g. [15]) and arises directly from the assumption of continuous re-equilibration of solid and liquid. Fractional melts are produced only if the solid does not re-equilibrate with the melt that passes through it (see Appendix A).

Short-lived radioactive nuclides, however, do not behave like stable elements, and the concentrations of  $^{230}\text{Th}$  and  $^{226}\text{Ra}$  in the melt can be greater than the concentration of a stable element with the same bulk partition coefficient (i.e. Eq. 13). For the example shown in Fig. 3b,c the amount of  $^{230}\text{Th}$  in the melt at the top of the column is  $\sim 13\%$  greater than if it were a stable element. Figure 4 shows the evolution of  $^{230}\text{Th}$  (and  $^{232}\text{Th}$ ) in both solid and liquid plotted on a standard equiline diagram [29].  $^{226}\text{Ra}$  shows an increase of  $\sim 250\%$ , even though the melt takes over ten half-lives of  $^{226}\text{Ra}$  to cross the column. These results show that more daughter material is actually being produced in the column than was brought in at the bottom. It is this new ingrown material that accounts for the excess activity ratios calculated at the surface (Fig. 3d).

This effect can be explained simply in terms of the relative residence times of each of the elements as was illustrated schematically in Fig. 2. Because individual elements have different transport velocities, they spend different amounts of time in the melting column. Here,  $^{238}\text{U}$  travels more slowly than  $^{230}\text{Th}$  which is slower than  $^{226}\text{Ra}$  and the additional residence times lead to excesses of daughter nuclides. The effects of transport can be separated from those of melting if we rewrite the melt concentrations as

$$c'_i = \alpha_i c'_{Bi} \quad (14)$$

where  $c'_{Bi}$  is the batch melt concentration expected for a stable element (Eq. 13), and  $\alpha_i$  is the enrichment factor due to radioactive decay. Substituting Eq. (14) into

Eq. (10) yields the simpler equation

$$\frac{d\alpha_i}{d\zeta} = \lambda_i d \left[ \frac{\alpha_{i-1}}{w_{eff}^{i-1}} - \frac{\alpha_i}{w_{eff}^i} \right] \quad (15)$$

which shows that the enrichment due to decay depends only on the relative velocities of the parent and daughter nuclides. Equation (15) can be solved for  $\alpha_i$  directly, however, it is numerically more stable to solve Eq. (10).

For a given degree of melting, the relative velocity of each element depends on the porosity, the upwelling rate of the solid and the relative affinity of each element for the solid phase, which in the simplest case is given by the partition coefficients. Figure 5 shows how changing the two principal physical parameters,  $\phi_{max}$  and  $W_0$ , affects the activity ratios ( $^{230}\text{Th}/^{238}\text{U}$ ) and ( $^{226}\text{Ra}/^{230}\text{Th}$ ) in the melt at the top of the column. For a fixed set of partition coefficients, the contours of the activity ratios have two different behaviours. In some regions of parameter space the activities depend primarily on the porosity while in others they depend primarily on the upwelling rate. These two different behaviours are controlled by whether the total extraction time of the daughter nuclide is long or short compared to its half-life. The extraction time for any element is the time it takes the element to traverse the melting region. The curves labeled  $t_c$  in Figs. 5a and 5b show an extraction time equal to approximately six half-lives of the daughter nuclide. After  $\sim 6$  half-lives, 99% of a given nuclide has decayed. Thus  $t_c$  corresponds to the longest time for which daughter nuclides present at the bottom of the column will still be present at the top. Any solution with combined  $W_0$  and  $\phi_{max}$  that plots above the curve  $t_c$ , has a shorter extraction time and nuclides can be sampled from the entire column. In this regime, activity ratios are sensitive to the upwelling velocity. Points that plot below the curve (e.g. slower upwelling rates), have extraction times longer than  $t_c$  and only nuclides formed in the upper part of the column are sampled at the surface. For these solutions, the activity ratios depend primarily on the porosity. Further analysis of Eq. (15) shows this result is the expected behaviour of the governing equations (Appendix A).

The behaviour of  $^{226}\text{Ra}$  is qualitatively the same as that for  $^{230}\text{Th}$ , but because these nuclides have very different half-lives and partition coefficients, they behave differently for the same values of  $\phi_{max}$  and  $W_0$ . The rectangular boxes in Fig. 5 show a range

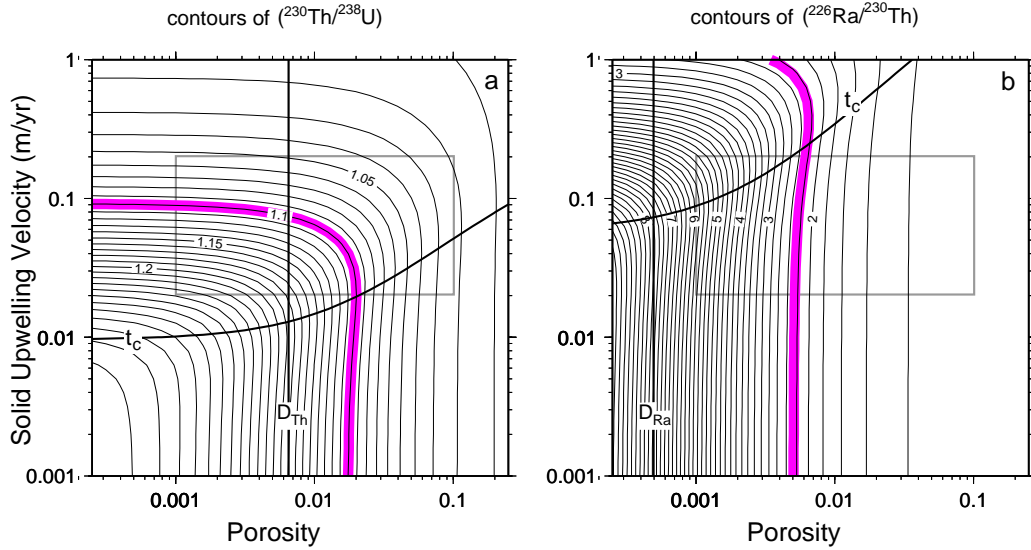


Figure 5: Effect of upwelling rate  $W_0$  and maximum porosity  $\phi_{max}$  on activity ratios calculated for melt at the top of the upwelling column (contours). The maximum degree of melting for all calculations is  $F_{max} = 0.25$ ,  $d = 50\text{km}$ , and the partition coefficients are  $D_U = 0.0086$ ,  $D_{Th} = 0.0065$  and  $D_{Ra} = 0.0005$  (a) contours of activity ratios for  $(^{230}\text{Th}/^{238}\text{U})$  (b) contours of  $(^{226}\text{Ra}/^{230}\text{Th})$ . The thick shaded contours mark the reference activity ratios  $(^{230}\text{Th}/^{238}\text{U}) = 1.1$  and  $(^{226}\text{Ra}/^{230}\text{Th}) = 2.25$  shown in Fig. 1. Note that for both  $^{230}\text{Th}$  and  $^{226}\text{Ra}$  there are two different regimes, one where the activity ratio is sensitive to upwelling velocity, the other is where the activity is only sensitive to the porosity. The location of the two regimes is controlled by the half-life of each daughter nuclide and the ratio of their partition coefficients to the porosity. In each plot, the vertical line marks the solutions where the maximum porosity is equal to the partition coefficient. The bold curved line marks the extraction time  $t_c = 6.64t_{1/2}$  (see text). The grey boxes mark values of  $W_0$  appropriate for moderate to fast spreading ridges and a range of plausible porosities. In this region, the thorium and radium contours are roughly orthogonal. Thus a small change in porosity can cause large changes in  $(^{226}\text{Ra}/^{230}\text{Th})$  with negligible changes in  $(^{230}\text{Th}/^{238}\text{U})$  which is consistent with observations (Fig. 1).

of porosities and upwelling velocities that are reasonable for moderate to fast spreading ridges. In this regime,  $^{230}\text{Th}$  excesses record ingrowth throughout the column while  $^{226}\text{Ra}$  excess are sensitive only to processes near the surface. Thus small variations in porosity can cause large changes in radium activity with negligible effects on the thorium excesses of the erupted melt.

Examination of Fig. 5 also shows how changing the values of the partition coefficients affects the activity ratios. Each plot has a maximum activity ratio that occurs for slow upwelling and small porosities. This maximum is the ratio of the parent and daughter partition coefficients. The positions of the contours in Fig. 5, however, are controlled by the ratio of the daughter partition coefficient to the porosity ( $D_{daughter}/\phi_{max}$ ). If the ratios of the partition coefficients remain the same but all the elements are more incompatible, then a smaller porosity is required to produce the same activity ratio.

Because  $^{230}\text{Th}$  is both a daughter and parent nuclide in the decay chain, combined measurements of  $(^{230}\text{Th}/^{238}\text{U})$  and  $(^{226}\text{Ra}/^{230}\text{Th})$  place stronger constraints on the model parameters than either measurement separately. However, because the  $^{230}\text{Th}$  and  $^{226}\text{Ra}$  excesses are produced in different regions of the melt column, this calculation shows that it is possible to produce large  $^{226}\text{Ra}$  excesses without requiring melt extraction times that are short compared to the half-life of  $^{226}\text{Ra}$ . While the actual values of the activity ratios are sensitive to the chosen parameters, the important conclusion of this calculation is that melt transport with melt-solid interaction can cause significant excesses of short lived isotopes.

## 4 Comparison to previous models

The behaviour of the simplest transport model is readily understood in terms of the relative residence times of parent and daughter elements in the melting system. Previous melting models can also be explained within

the framework of residence times, and nearly all the differences in behaviour and implications of the models can be traced to differences in the processes that govern the residence times of each element. This section highlights the subtle differences between all of the models and suggests that all else being equal, the calculations that include melt transport with melt-solid interaction produce the largest thorium and radium excesses in a physically reasonable system.

The earliest models (e.g. [30]) that attempt to account for  $^{230}\text{Th}$  excesses actually have no difference in residence times between uranium and thorium, and simply explain the different activity ratios by instantaneous chemical fractionation of parent from daughter. Chemical fractionation, however, only works when the degree of melting  $F$  is comparable to the bulk partition coefficients  $D$ . This mechanism is clearly not viable at ridges where the average degree of melting is at least an order of magnitude greater than all of the partition coefficients of the  $^{238}\text{U}$  series nuclides.

More sophisticated “dynamic melting” models [7, 8] consider one-dimensional, steady-state melting columns with a constant melting rate and a single set of partition coefficients. In these respects, such models are similar to ours. However, the dynamic models do not include melt migration and, furthermore, are effectively fractional melting calculations. Figure 6 illustrates the behaviour of the dynamic melting models. These calculations assume that the entire column has a constant porosity of melt that is in chemical equilibrium with the solid. Any melt that is produced in excess of this constant porosity is ‘extracted’ into a second chemically isolated reservoir where it is assumed to be instantaneously mixed and erupted.

In these calculations, excess daughter is also produced by decay of the parent, however, the relative residence times are controlled by the melting rate and not by the transport time. If the parent is more compatible than the daughter, it will spend a longer time in the solid before it is “pushed” into the liquid by melting. If the melting rate is sufficiently slow to allow the parent to decay, the longer residence time in the solid will produce excesses in the same manner as in our calculation. Once the extracted melt enters the chemically isolated reservoir, however, all elements travel at the melt velocity and thus have the same residence time. Any excess in the second reservoir that is produced by slow melting can only decay back to secular equilibrium. Because these dynamic melting models are

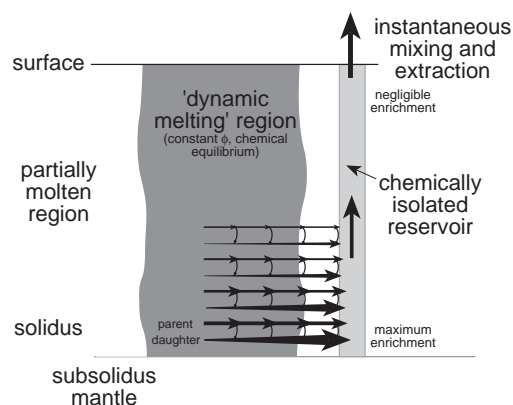


Figure 6: A cartoon illustrating the behaviour of “dynamic melting” models. These models propose two reservoirs. The first is the melting region where the solid maintains chemical equilibrium with a small constant porosity  $\phi_{eq}$ . Any melt that is produced in excess of this equilibration porosity is ‘extracted’ into the second reservoir which is chemically isolated from the solid. Physically, this second reservoir could be a network of veins or dikes in which the melt does not re-equilibrate with the solid (e.g. [19]). In this second reservoir, any excess produced by slow melting can only decay towards secular equilibrium. The simplest dynamic melting models [7, 8] do not include melt extraction and simply mix the contents of the second reservoir from all heights in the column and assume instantaneous eruption at the surface. For small  $\phi_{eq}$  (i.e.  $\phi_{eq} \ll F$ ) these calculations are essentially fractional melting calculations and incompatible elements are stripped from the melting region during the first  $F \sim D_i$  degree of melting. Thus nearly all of the ingrowth of daughter nuclides occurs at the bottom of the column and requires rapid extraction to be preserved to the surface.

effectively fractional melting calculations, the incompatible elements are efficiently stripped from the solid within the first few percent of melting. Thus nearly all of the enrichment in both thorium and radium occurs at the bottom of the column.

While the differences between our calculation and the dynamic melting models may not appear to be great, these models actually lead to very different interpretations of the data. Our calculation produces excesses at all levels in the column, with thorium preserving excesses produced at the bottom of the melting region and radium recording shallow level interaction and transport. Because the radium excesses are produced near the surface, our model actually places no constraints on the minimum extraction time of melt.

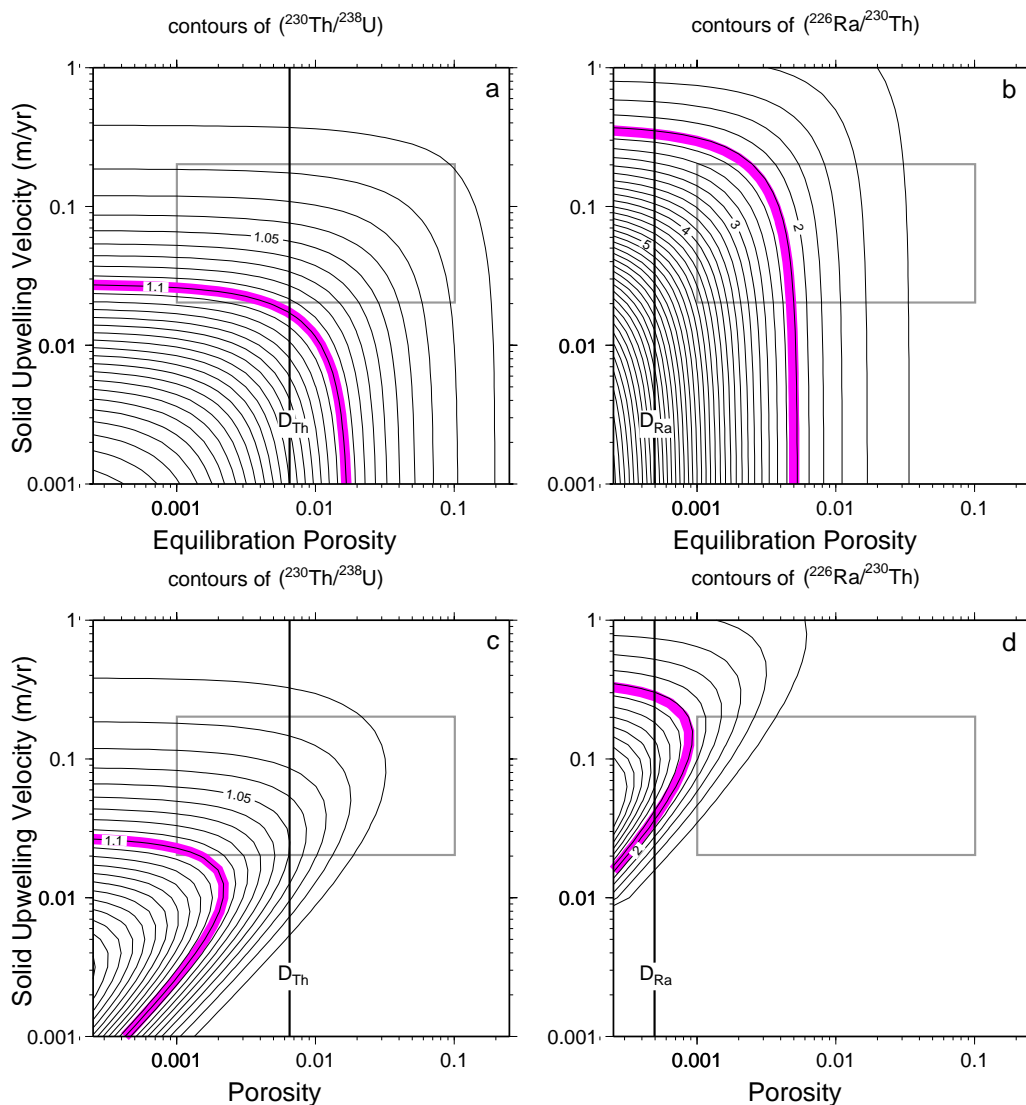


Figure 7: (a, b) Contours of activity ratios for models that assume instantaneous melt transport [7, 8]. This figure shows the solution of the “dynamic melting calculation” given in [8] for the same partition coefficients as used in Fig. 5. In this calculation the “equilibration porosity”  $\phi_{eq}$  is the small volume of liquid that remains in chemical equilibrium with the solid.  $\phi_{eq}$  is not directly comparable to the porosity in the transport calculations but has similar effects for radioactive disequilibrium when melt transport is instantaneous. (c, d) The effects of adding melt transport to dynamic melting models. This calculation uses the same fluid dynamics as Fig. 5 but assumes that the solid melts fractionally and does not interact with the melt that passes through it (see Appendix A). Pure fractional melting corresponds to  $\phi_{eq} = 0$  in Fig. 7a,b and produces maximum radioactive disequilibria in dynamic melting models. Once transport is included, however, any excesses that are produced by melting at the bottom of the column decay during transit to the surface. Hence 7c,d shows smaller  $^{230}\text{Th}$  and negligible  $^{226}\text{Ra}$  excesses for the same parameters as Fig. 5. The shaded grey contours are for the reference values,  $(^{230}\text{Th}/^{238}\text{U}) = 1.1$ ,  $(^{226}\text{Ra}/^{230}\text{Th}) = 2.25$  shown in Fig. 1.

The dynamic melting models, however, require rapid extraction because nearly all of the significant excesses are produced at the bottom of the column, and after fractionation are chemically isolated from their source and can only decay during transport.

It should be reiterated that the dynamic melting calculations assume instantaneous transport and mixing of melts from all depths. With these somewhat arbitrary assumptions, the dynamic melting calculations can produce average excesses that are comparable to those produced in our model. Figure 7a,b shows the activity ratios of the mixed melts using the same partition coefficients, melting depth and overall degree of melting as Fig. 5. Qualitatively, the solutions are similar, but for a given upwelling rate (melting rate) the dynamic melting calculation gives lower excesses. Even these slightly smaller excesses are maxima, however, since this solution assumes instantaneous extraction.

Using the fluid dynamic framework developed in section 2, we can add the effects of melt transport to the dynamic melting calculations (see Appendix for details). Specifically, Fig. 7c,d shows the activities of melts erupted at the top of a column where the solid has undergone pure fractional melting and the melt that is produced segregates into a series of veins that do not interact with the solid through which they pass. The transport in these veins can still be described by Darcy's law (see [19]) and so the melt transport times in Figs. 5 and 7c,d are identical for a given porosity and upwelling rate. As is clear from Fig. 7c,d, once transport times are calculated for fractional (or near fractional) melting models, only small  $^{230}\text{Th}$  and negligible  $^{226}\text{Ra}$  excesses can be preserved in melts at the top of the column (see also [31]). Similar problems were noted for the "accumulated continuous melting" model of Williams and Gill [8].

Figures 5 and 7c,d represent the end-member solutions for one-dimensional melting columns with transport and "equilibrium melting." By equilibrium melting, we mean that there is full volume chemical equilibrium between the melting minerals and the instantaneous melts that are produced. Both "batch" and "fractional" melting models are examples of equilibrium melting, the only difference between them is the volume of melt that re-equilibrates with the solid. Similarly, the only difference between Figs. 5 and 7c,d is whether the melt and solid remain in chemical equilibrium during *transport*. Figure 5 assumes that the solid and liquid re-equilibrate throughout the column,

while Figure 7c,d assumes there is no chemical interaction during transport.

The basic requirements for maintaining chemical equilibrium during magma migration are discussed by Spiegelman and Kenyon [19] who suggest that the ability to maintain chemical equilibrium is very sensitive to the microscopic distribution of melt and solid. It should be noted, however, that the scaling argument presented by Spiegelman and Kenyon represents a worst case scenario which assumes that the melt is distributed in veins or channels separated by regions of pure solid. Given the low values of measured diffusivities in mantle minerals (e.g.  $\mathcal{D}^s \sim 10^{-16} \text{ m}^2 \text{ s}^{-1}$  at  $1240^\circ\text{C}$  for U in cpx [32]), it does not require a very large vein spacing before the interior of the solid regions cannot communicate with the melt in the channels. However, because the diffusivity of trace elements in the melt is orders of magnitude larger than that in the solid ( $\mathcal{D}^f \sim 10^{-10}\text{--}10^{-11} \text{ m}^2 \text{ s}^{-1}$  [33]) even a very small volume of interconnected melt along the grain edges can significantly enhance the effective diffusivity of the inter-channel regions. Recent experiments on two-phase aggregates [34, 35] suggest that surface energy effects will maintain such a network because nature abhors a dry grain edge. Spiegelman and Kenyon did not account for such a melt network in their calculations. Furthermore, the effects of deformation in a partially molten upper mantle could possibly increase the effective solid diffusivities over those measured in a static crystal. Thus a better understanding of the microscopic properties of melt-solid aggregates is required before we can determine where the transition from equilibrium to disequilibrium transport occurs.

Grain scale processes also control the "disequilibrium melting" models that have been recently presented [9, 36]. While only Qin [9] has explicitly calculated the behaviour of U-series nuclides, both models make identical assumptions about the microscopic mechanics of melting. These two models assume that the solid is composed of spherical grains where the surface of each grain is in chemical equilibrium with the melt phase but the interior can only equilibrate with the melt by solid diffusion. Most importantly, these models assume that the individual crystals melt much like peeling layers off an onion. Such "onion skin" melting leads to disequilibrium melting when the crystal surface retreats faster than an element can diffuse into the grain interior. All of the effects of

these models rest on this assumption of how individual grains melt, which again is unclear in an actively deforming mantle. Nevertheless, disequilibrium melting models provide a useful description of an end-member process.

The principal consequence of these disequilibrium melting models is that the effective partition coefficients of all elements tend to unity because the melt that is produced has nearly the same composition as the crystal. Thus while the effective partition coefficient of incompatible elements is much larger than in equilibrium, the amount of fractionation between elements diminishes unless they have significantly different diffusivities. Even so, the scaling parameters in [9, 36] suggest that to produce significant disequilibrium during melting requires that melting rates be  $\sim 2$  orders of magnitude larger than those estimated by Eq. (4). At these fast melting rates there is little time for additional ingrowth of daughter nuclides and this calculation is therefore analogous to the earliest models (e.g. [30]) where fractionation is purely chemical. Thus the principal effect of disequilibrium melting controlled by solid state diffusion is simply to raise the effective partition coefficients.

## 5 Discussion

By comparing the quantitative results of the available models, the previous sections show that melt transport with interaction between melt and solid throughout the melting region produces the largest radiogenic excesses for the same physical parameters. However, it is important to address how well our calculation can explain the observed excesses in mid-ocean ridge basalts.

The principal simplification in all of the models discussed so far is that the bulk partition coefficients are constant throughout the melting column. In order to generate the radiogenic excesses observed in MORB, the equilibrium melting models require that uranium is more compatible than thorium, which is more compatible than radium. Recent experiments show that, of the major mantle minerals, only garnet can produce significant  $^{230}\text{Th}$  excesses by equilibrium partitioning ( $D_U^{gar} \sim 10D_{Th}^{gar}$  [37, 38]). Olivine and opx have insignificant partition coefficients for U and Th [26] while uranium is actually less compatible than thorium in cpx [23-28]. Modeling of Lu/Hf systematics also suggests that some melting occurs in the presence of garnet [39] during MORB genesis. Garnet, how-

ever, is only stable at depths greater than  $\sim 60\text{km}$  [40-42] while the majority of MORB melting is thought to occur at shallower depths. Thus at least two sets of bulk partition coefficients are needed to adequately represent the markedly different behaviour of U and Th during MORB melting.

This additional complexity can be quantified by simply extending the single stage melting calculations to a two-stage model where the melting column now has two sets of partition coefficients that are consistent with the new experimental data. Hence, the bottom portion of the column is given bulk partition coefficients appropriate for melting in the garnet stability field, while the upper portion is given bulk partition coefficients suitable for melting in the spinel stability field. The partitioning behaviour of radium is still poorly constrained and will be assumed to be constant with height. However, as long as  $D_{Ra} \lesssim 0.1D_{Th}$  then its actual value makes little difference to the radium activity ratios as these are controlled principally by the partitioning of thorium. Experiments on Ba, used as an analogue for Ra, show that  $D_{Ba}/D_{Th} \sim 0.1$  [26, 28].

Figure 8 shows two end-member solutions for such a two layer column where melting begins at 80 km and the garnet-spinel transition occurs  $\sim 60\text{km}$  [40]. For simplicity the melting rate is assumed to be constant throughout the column. Figure 8a shows the solution where the melt re-equilibrates with the solid throughout the column. While this solution is somewhat more complicated than the one-stage model, the essential behaviour is the same. Even though melt-solid interaction in the upper layer will tend to drive ( $^{230}\text{Th}/^{238}\text{U}$ ) activity ratios to values  $< 1$ , because of the relatively long half-life of  $^{230}\text{Th}$ , any excesses produced in the lower layer can be preserved to the surface as long as the total extraction time is less than  $t_c$ . Only the very slowest extraction times will produce activity ratios less than one. Radium, however, is still assumed to be more incompatible than thorium throughout the column and records the relative residence times of  $^{230}\text{Th}$  and  $^{226}\text{Ra}$  near the surface. In contrast, Fig. 8b shows the solution for fractional melting and “disequilibrium transport.” Again ( $^{230}\text{Th}/^{238}\text{U}$ ) activities greater than one are produced because nearly all of the  $^{238}\text{U}$  series elements are fractionated within the first  $\sim 1\%$  of melting (approximately the lowest 2–3 km in the column) and therefore are only affected by garnet partitioning. The radium

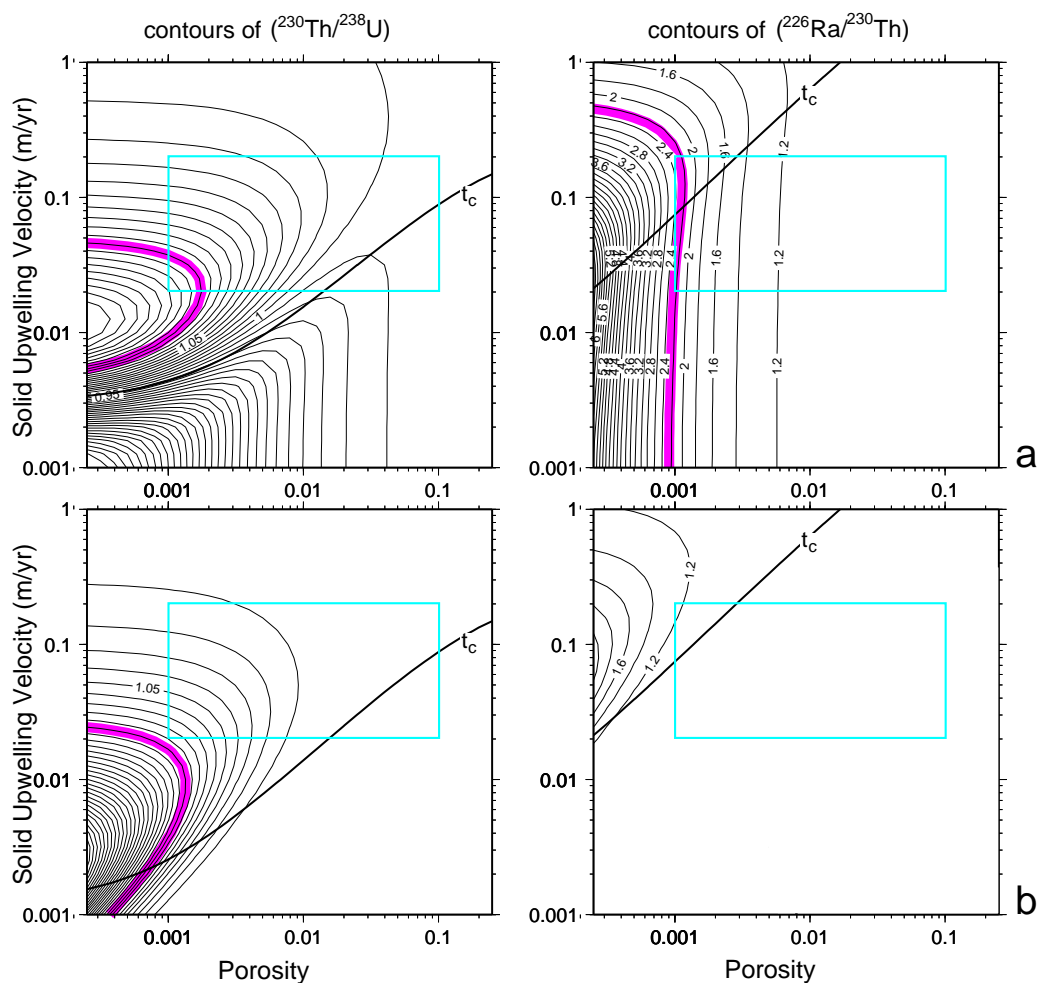


Figure 8: A comparison of two end-member calculations for a two-stage melting column with equilibrium bulk partition coefficients consistent with recent partitioning experiments. In both calculations the melting column is 80 km deep. Partition coefficients for the lower 20km are  $D_U = 0.00162$ ,  $D_{Th} = 0.00074$  ( $\sim 10\%$  garnet plus  $10\%$  cpx). The upper 60 km has  $D_U = 0.0006$ ,  $D_{Th} = 0.000975$  ( $15\%$  cpx).  $D_{Ra}$  is still unconstrained and is chosen to be  $= 10^{-5}$  for the entire column. Shaded contours show the reference values  $(^{230}\text{Th}/^{238}\text{U}) = 1.1$ ,  $(^{226}\text{Ra}/^{230}\text{Th}) = 2.25$ . (a) “equilibrium” transport calculation with melt and solid interaction throughout the column. Because  $^{230}\text{Th}$  can remember interaction with garnet,  $^{230}\text{Th}$  excesses can still be produced if the extraction time is less than  $t_c$ . Only slower extraction will produce  $(^{230}\text{Th}/^{238}\text{U}) < 1$ . Radium behaves exactly as in the single-stage calculation and only records the ratio of residence times near the top of the column. (b) Fractional melting and disequilibrium transport produce smaller  $^{230}\text{Th}$  and negligible  $^{226}\text{Ra}$  excesses for the same parameters.

excesses, however, are also produced at the bottom of the column and will decay before they can be erupted unless the melt moves sufficiently fast for the radium to traverse 80km within its half-life (see below).

Between these two solutions lie a large number of related models. In addition to varying the partition coefficients or the depth to the garnet-spinel transition, we could also vary the melting rate within the column, change the degree of re-equilibration of melt and solid as a function of height or even extend the calculation to two-dimensional flow models. Appendix A shows how to quantify these effects, but because of the large number of adjustable parameters and scenarios, we have not explored these more complicated models in any detail. The important point to stress is that it is only differences in the total residence time of each element that controls the amount of secular disequilibrium. Thus it is not particularly difficult to produce  $^{230}\text{Th}$  excesses if some melting occurs in the presence of garnet as the half-life of  $^{230}\text{Th}$  is sufficiently long to “remember” the garnet field. The principal constraint on all of these models is to produce both  $^{230}\text{Th}$  and  $^{226}\text{Ra}$  excesses for the same physical regime.

The primary difficulty with the new partitioning data is the very small values of the partition coefficients. With values as small as those suggested, it is difficult for *any* of the models to produce large  $^{226}\text{Ra}$  excesses using “reasonable” melting rates and porosities. Dynamic melting models require slower melting rates to offset the efficient stripping of elements due to fractional melting. These models, however also require very fast extraction rates to preserve  $^{226}\text{Ra}$  excesses to the surface. The combination of slow melt production rates and fast extraction rates imply that there can only be a very small residual porosity in steady-state. Examination of Fig. 8b or Eq. (5) shows that conservation of mass requires residual porosities  $\phi \lesssim 10^{-4}$  throughout most of the melting column if the extraction time is required to be one half-life of  $^{226}\text{Ra}$ . Melt transport with melt-solid interaction, however also needs small porosities comparable to the partition coefficient of thorium *if* the different effective velocities are controlled solely by equilibrium bulk partitioning. At the small porosities required to generate large  $^{226}\text{Ra}$  excesses, the melt velocity is sufficiently high that full volume chemical equilibration may not be maintained if the effective diffusivity of the solid is small. These difficulties lead us to several alternative suggestions to account for the ob-

served  $^{238}\text{U}$ -series excesses in Fig. 1.

Perhaps the simplest explanation for the large  $^{226}\text{Ra}$  excesses in MORB is that they are not primary magmatic features and it has yet to be shown conclusively that the  $^{226}\text{Ra}$  excesses are not the result of near surface contamination. Nevertheless, all of the analyses shown in Fig. 1 were made on carefully picked and processed, fresh MORB glasses. Furthermore, off axial glasses show ( $^{226}\text{Ra}/^{230}\text{Th}$ ) equilibrium that is consistent with ages inferred from paleomagnetically determined spreading rates [6]. Thus any contamination would need to occur prior to quenching. Assimilation of barite, which is precipitated from hydrothermal systems at ridge axes with extreme ( $^{226}\text{Ra}/^{230}\text{Th}$ ) ratios (e.g. [43]), could account for the large  $^{226}\text{Ra}$  excesses shown in Fig. 1. However, there are further chemical signatures associated with barite assimilation and a detailed study is needed to evaluate if such parameters correlate with  $^{226}\text{Ra}$  excesses. Since it is the combined thorium and radium data that places the strongest constraints on the rates of mantle processes, if the radium is not coupled to the thorium, then much of the fun in this system is lost.

If the  $^{226}\text{Ra}$  activities are primary, however, we still need a mechanism that can produce large  $^{226}\text{Ra}$  excesses and still be consistent with the new partitioning data. It is important to stress that though we have used bulk partition coefficients to control the effective velocities of elements in these simplest models, the only really important requirement for radioactive disequilibrium is that parent and daughter nuclides travel at different speeds. We suggest that other processes may also produce differential transport velocities that can lead to secular disequilibrium. For example, one possibility is that different degrees of surface adsorption or interaction with crystal grain boundaries could also cause variable transport velocities. While this suggestion is admittedly speculative, it does have several intriguing features that we feel merit some further discussion. First, unlike volume partitioning, surface or grain boundary effects need not be isolated to a few specific mineral phases but could occur on all melt-solid interfaces. Thus even if the principal phase controlling bulk partitioning is exhausted by melting, surface effects could still operate. The quantitative results of section 3 show that large radiogenic excesses do not require large amounts of melt-solid interaction (i.e. effective partition coefficients do not need to exceed  $\sim 0.01$ ). Second, if the residence time of ele-

ments is controlled by surface processes, then these effects would only be noticeable in the ratios of short-lived radiogenic nuclides which are sensitive to transport times. Relatively small amounts of surface interaction could have a significant effect on radioactive disequilibrium yet have a negligible effect on the ratios of stable incompatible elements. Thus it may be possible to produce secular disequilibrium in MORB even if the mantle undergoes fractional melting as is suggested by modeling of other geochemical systems [44-46].

Another possibility for enhancing differential residence times is, if in addition to veins or channels, the melt exists as a connected grain boundary phase as was discussed in the previous section. In the simplest calculations, it is assumed that all melt traveled at velocity  $w$  and all the solid traveled at velocity  $W$ . However, if there are actually two porosities, one governing the volume of melt in the channels and one governing the interstitial melt phase that travels near the solid velocity, then it is possible for elements to travel at different velocities if there is some interaction between the veins and the interstitial melt.

These suggestions clearly need to be addressed quantitatively. However, as long as the different elements have different residence times, excesses will result. At this point we acknowledge that the magnitude of these processes are unconstrained, largely because of our lack of information about the surface and transport properties of aggregates of mantle minerals, and of the microscopic physics of melting in a deforming upper mantle. Further experimental evidence is required to evaluate these suggestions.

## 6 Conclusions

We have shown that melt transport with interaction between the solid and liquid can have large effects on the abundances of short-lived radionuclides by changing the residence times of parent and daughter elements. As long as the parent spends more time in the melting system than the daughter, excess daughter will be produced. For the same parameters, the transport calculations with solid-liquid interaction produce larger excesses than dynamic melting or disequilibrium transport models and do not require rapid melt extraction. For (favourable) conditions, our calculations can produce both  $^{230}\text{Th}$  and  $^{226}\text{Ra}$  excesses that are comparable to those observed at moderate to fast spreading ridges using physically reasonable transport veloci-

ties. The melt transport models can be extended to include the results of recent partitioning experiments, but results suggest that additional processes may still be required to fully explain the observations.

**Acknowledgements** The authors are very grateful to K. Rubin for allowing us to use unpublished data and for enthusiastic discussions. We would also like to thank J. Gill, T. LaTourrette and K. Rubin for useful reviews. Additional insightful comments were provided by T. Plank, B. Bourdon, V. Salters, R. Oxburgh and D. House. This is Lamont-Doherty Earth Observatory contribution 5072.

## References

- 1 M. Condomines, C. Hémond, and C.J. Allègre, U-Th-Ra radioactive disequilibria and magmatic processes, *Earth Planet. Sci. Lett.*, 90, 243–262, 1988.
- 2 J.B. Gill and M. Condomines, Short-lived radioactivity and magma genesis, *Science*, 257, 1368–1376, 1992.
- 3 K.H. Rubin and J.D. Macdougall,  $^{226}\text{Ra}$  excesses in mid-ocean-ridge basalts and mantle melting, *Nature*, 335, 158–161, 1988.
- 4 I. Reinitz and K.K. Turekian,  $^{230}\text{Th}/^{238}\text{U}$  and  $^{226}\text{Ra}/^{230}\text{Th}$  fractionation in young basaltic glasses from the East Pacific Rise, *Earth Planet. Sci. Lett.*, 94, 199–207, 1989.
- 5 K.H. Rubin, J.D. Macdougall, J.M. Sinton, and J.J. Mahoney,  $^{238}\text{U}$ - $^{230}\text{Th}$ - $^{226}\text{Ra}$  radioactive disequilibrium and Th isotopes in EPR MORB from 13°S–23°S: axial variations in lava age, source chemistry, trace element fractionation and magmatic transport, *Earth Planet. Sci. Lett.*, (in review), 1992.
- 6 A.M. Volpe and S.J. Goldstein,  $^{226}\text{Ra}$ - $^{230}\text{Th}$  disequilibrium in axial and off-axis mid-ocean ridge basalts, *Geochim. Cosmochim. Acta*, 57(6), 1233–1242, 1993.
- 7 D. McKenzie,  $^{230}\text{Th}$ - $^{238}\text{U}$  disequilibrium and the melting process beneath ridge axes, *Earth Planet. Sci. Lett.*, 74, 81–91, 1985.
- 8 R.W. Williams and J.B. Gill, Effects of partial melting on the  $^{238}\text{U}$  decay series, *Geochim. Cosmochim. Acta*, 53, 1607–1619, 1989.
- 9 Z. Qin, Disequilibrium partial melting model and

- implications for the fractionations of trace elements during mantle melting, *Earth Planet. Sci. Lett.*, 112, 75–90, 1992.
- 10 O. Navon and E. Stolper, Geochemical consequences of melt percolation: the upper mantle as a chromatographic column, *J. Geol.*, 95, 285–307, 1987.
- 11 M. Bickle and D. McKenzie, The transport of heat and matter by fluids during metamorphism, *Contrib. Mineral. Petrol.*, 95, 384–392, 1987.
- 12 D. McKenzie, The generation and compaction of partially molten rock, *J. Petrol.*, 25, 713–765, 1984.
- 13 D. Scott and D. Stevenson, Magma solitons, *Geophys. Res. Lett.*, 11, 1161–1164, 1984.
- 14 D. Scott and D. Stevenson, Magma ascent by porous flow, *J. Geophys. Res.*, 91, 9283–9296, 1986.
- 15 N. Ribe, The generation and composition of partial melts in the earth's mantle, *Earth Planet. Sci. Lett.*, 73, 361–376, 1985.
- 16 M. Spiegelman, Flow in deformable porous media. Part 1. Simple analysis, *J. Fluid Mech.*, 247, 17–38, 1993.
- 17 M. Spiegelman, Flow in deformable porous media. Part 2. Numerical analysis — the relationship between shock waves and solitary waves, *J. Fluid Mech.*, 247, 39–63, 1993.
- 18 N. Ribe, The deformation and compaction of partially molten zones, *Geophys. J. R. Astron. Soc.*, 83, 137–152, 1985.
- 19 M. Spiegelman and P. Kenyon, The requirements for chemical disequilibrium during magma migration, *Earth Planet. Sci. Lett.*, 109, 611–620, 1992.
- 20 M. Cheadle, Properties of texturally equilibrated two-phase aggregates, Ph. D., University of Cambridge, 1989.
- 21 J. Ahern and D. Turcotte, Magma migration beneath an ocean ridge, *Earth Planet. Sci. Lett.*, 45, 115–122, 1979.
- 22 W.H. Press, B.P. Flannery, S.A. Teukolsky, and W.T. Vetterling, *Numerical Recipes*, Cambridge University Press, Cambridge, U.K., 1986.
- 23 M. Seitz, Uranium and thorium partitioning in diopside-melt and whitlockite-melt systems, *Carnegie Inst. Wash. Yearb.*, 72, 581–586, 1973.
- 24 T. Benjamin, W.R. Heuser, D.S. Burnett, and M.G. Seitz, Actinide crystal-liquid partitioning for clinopyroxene and  $\text{Ca}_3(\text{PO}_4)_2$ , *Geochim. Cosmochim. Acta*, 44, 1251–1264, 1980.
- 25 T.Z. LaTourrette and D.S. Burnett, Experimental determination of U and Th partitioning between clinopyroxene and natural and synthetic basaltic liquid, *Earth Planet. Sci. Lett.*, 110, 227–244, 1992.
- 26 P.D. Beattie, The generation of uranium series disequilibria by partial melting of spinel peridotite: Constraints from partitioning studies, *Earth Planet. Sci. Lett.*, (in press), 1993.
- 27 E.H. Hauri, T.P. Wagner, S.R. Hart, and T.L. Grove, Experimental and natural partitioning of U, Th and Pb between cpx, garnet and basaltic melts: implications for Th/U, Ce/Pb and Pb isotope evolution in the upper mantle, *EOS, Trans. Amer. Geophys. Union*, 74, 340, 1993.
- 28 C.C. Lundstrom, H.F. Shaw, D.L. Phinney, F.J. Ryerson, J.B. Gill, and Q. Williams, New U-Th-Ba partition coefficients between chromian diopside and haplobasaltic melts, *EOS, Trans. Amer. Geophys. Union*, 74, 341, 1993.
- 29 C.J. Allègre,  $^{230}\text{Th}$  dating of volcanic rocks. A comment, *Earth Planet. Sci. Lett.*, 3, 338, 1968.
- 30 C.J. Allègre and M. Condomines, Basalt genesis and mantle structure studied through Th-isotopic geochemistry, *Nature*, 299, 21–24, 1982.
- 31 B. Bourdon, A bidimensional model for U decay series disequilibria in MORB, *EOS, Trans. Amer. Geophys. Union*, 72(17), 295, 1991.
- 32 M. Seitz, Uranium and thorium diffusion in diopside and fluorapatite, *Carnegie Inst. Wash. Yearb.*, 72, 586–588, 1973.
- 33 A.W. Hofmann, Diffusion in natural silicate melts: a critical review, in: *Physics of Magmatic Processes*, E. Hargraves, Editor, Princeton University Press, Princeton. p. 385–417, 1980.
- 34 G.N. Riley and D.L. Kohlstedt, Kinetics of melt migration in upper mantle-type rocks, *Earth Planet. Sci. Lett.*, 105, 500–521, 1991.
- 35 M.J. Daines and D.L. Kohlstedt, A laboratory study

- of melt migration, *Phil. Trans. R. Soc. Lond. A*, 342, 43–52, 1993.
- 36 H. Iwamori, Dynamic disequilibrium melting model with porous flow and diffusion-controlled chemical equilibration, *Earth Planet. Sci. Lett.*, 114, 301–313, 1993.
- 37 P.D. Beattie, Uranium-thorium disequilibria and partitioning on melting of garnet peridotite, *Nature*, (in press), 1993.
- 38 T.Z. LaTourrette, A.K. Kennedy, and J.G. Wasserburg, U and Th partitioning between garnet and silicate melt, *EOS, Trans. Amer. Geophys. Union*, 73(43), 607, 1992.
- 39 B. Salters and S. Hart, The hafnium paradox and the role of garnet in the source of mid-ocean ridge basalts, *Nature*, 342, 420–422, 1989.
- 40 R.J. Kinzler, Mantle melting processes at the spinel-garnet transition, *EOS, Trans. Amer. Geophys. Union*, 73(43), 615, 1992.
- 41 H.S.C. O’Niell, The transition between spinel lherzolite and garnet lherzolite, and its use as a geobarometer, *Contrib. Mineral. Petrol.*, 77, 185–194, 1981.
- 42 K.G. Nickel, Phase equilibria in the system  $\text{SiO}_2\text{-MgO-Al}_2\text{O}_3\text{-CaO-Cr}_2\text{O}_3$  (SMACCR) and their bearing on spinel/garnet lherzolite relationships, *Neues Jahrb. Miner. Abh.*, 155, 259–287, 1986.
- 43 D. Stakes and W.S. Moore, Evolution of hydrothermal activity on the Juan de Fuca Ridge: observations, mineral ages and Ra isotope ratios, *J. Geophys. Res.*, 96, 21,739–21,752, 1991.
- 44 K. Johnson, H. Dick, and N. Shimizu, Melting in the oceanic upper mantle: An ion microprobe study of diopsides in abyssal peridotites, *J. Geophys. Res.*, 95, 2661–2678, 1990.
- 45 T.R. Elliott, C.J. Hawkesworth, and K. Grönvold, Dynamic melting of the Iceland plume, *Nature*, 351, 201–206, 1991.
- 46 C.H. Langmuir, E. Klein, and T. Plank, Petrological systematics of mid-oceanic ridge basalts: constraints on melt generation beneath ocean ridges, *AGU monograph*, 71, 183–280, 1992.
- 47 M. Spiegelman, Passive vs. active flow? Only the tracers know..., *EOS, Trans. Amer. Geophys. U.*,

73(14), 290, 1992.

- 48 T. Plank and C.H. Langmuir, Effects of the melting regime on the composition of the oceanic crust, *J. Geophys. Res.*, 97, 19,749–19,770, 1992.

## A Appendix: Additional analysis

Section 2 presented the specific equations for a one-dimensional steady-state upwelling column with constant melting rate, equilibrium melting and transport with a single set of constant partition coefficients. This appendix shows how to generalize this model to allow for variable melting rates, non-constant partition coefficients and disequilibrium melt transport. It also presents a simple approximate solution to Eq. (15) to demonstrate that the numerical results are correct.

### A.1 General equations for one-dimensional, steady-state columns

Conservation of mass for a two-phase system of melt and solid is

$$\frac{\partial(\rho_f \phi)}{\partial t} + \nabla \cdot (\rho_f \phi \mathbf{v}) = \Gamma \quad (16)$$

$$\frac{\partial[\rho_s(1 - \phi)]}{\partial t} + \nabla \cdot [\rho_s(1 - \phi)\mathbf{V}] = -\Gamma \quad (17)$$

where  $\Gamma$  is the melting rate which can be a function of height and time (see Table 1 for notation; see [12] for the derivation of conservation equations). In one dimensional steady-state melting columns, Eqs. (16) and (17) can be integrated directly using the boundary conditions at the base of the column ( $z = 0$ ) that the porosity  $\phi = 0$ , and the solid upwelling velocity is  $W_0$  to give

$$\rho_f \phi w = \int_0^z \Gamma dz \quad (18)$$

$$\rho_s(1 - \phi)W = \rho_s W_0 - \int_0^z \Gamma dz \quad (19)$$

where in steady-state  $\Gamma = \Gamma(z)$  i.e. the melting rate is only a function of height. Equation (18) states that in steady-state, the melt flux,  $\rho_f \phi w$  at any height in the column simply balances the total melt production up to that height. Now, by definition, the degree of melting that the solid experiences in steady-state is

$$F(z) = \frac{\int_0^z \Gamma dz}{\rho_s W_0} \quad (20)$$

which is the ratio of the total melt production flux to the flux of solid that enters the base of the column. Therefore if  $\Gamma$  is assumed to be constant throughout the melting region and the maximum degree of melting at height  $d$  is  $F_{max}$  then Eq. (20) shows that the melting rate must be  $\Gamma = \rho_s W_0 F_{max}/d$  which is identical to Eq. (4). If the melting rate is variable with height, then Eq. (20) can still be used to derive the degree of melting and Eqs. (18)–(19) become

$$\rho_f \phi w = \rho_s W_0 F \quad (21)$$

$$\rho_s (1 - \phi) W = \rho_s W_0 (1 - F) \quad (22)$$

and  $F = F(z)$  (see also [15]). Given any functional relationship between porosity and melt and solid velocities, Eqs. (21)–(22) can be solved to give the porosity as a function of height. In the simplest model problem, we have used Darcy's law driven solely by the density difference between melt and solid with a power law relationship between porosity and permeability. For a more general set of equations governing the separation of melt from solid in multi-dimensions see [12–14, 16, 17].

## A.2 Equilibrium chemical transport with non-constant bulk distribution coefficients

Using Eqs. (21)–(22) with Eq. (1) and rewriting Eq. (20) as  $\Gamma = \rho_s W_0 dF/dz$ , then the general equation for the evolution of radiogenic elements in a one-dimensional, steady-state column where the element maintain chemical equilibrium at all times is

$$\frac{dc_i^f}{dz} = \frac{-c_i^f}{D_i + (1 - D_i)F} \frac{d}{dz} [D_i + (1 - D_i)F] + \frac{[\lambda_{i-1} [\rho_f \phi + \rho_s (1 - \phi) D_{i-1}] c_{i-1}^f - \lambda_i [\rho_f \phi + \rho_s (1 - \phi) D_i] c_i^f]}{\rho_s W_0 [D_i + (1 - D_i)F]}$$

where  $F$ ,  $D_i$  are now functions of position  $z$ . The set of equations in (23) can be solved for  $c_i^f$  by the same numerical schemes used for constant melting rate and partition coefficients (although in general it is usually numerically more stable to solve for  $U_i = \ln(c_i^f/c_{i0}^f)$  than to solve for the  $c_i^f$ 's directly). Note also that if the elements are stable ( $\lambda_i = 0$  for all  $i$ ), then Eq. (23) can be solved analytically to produce the equation for batch melting (Eq. 13) independent of porosity or melt separation.

## A.3 Disequilibrium chemical transport with non-constant bulk distribution coefficients

Equation (1) presumes that the melt and the solid matrix re-equilibrate instantly throughout the melting column, i.e. the solid interacts with all the melt that passes through it. This feature results in melt compositions that are equivalent to batch melts for stable elements. At the opposite extreme it is straightforward to derive equations for a system where the solid melts to produce a melt that is locally in equilibrium with the solid; however, the solid does not interact chemically with melts that are produced lower in the column. Physically this corresponds to melt that can segregate into chemically isolated channels or veins (see [19]). In this case conservation of mass for trace element  $i$  must be calculated in both the solid and the liquid and the generalization of Eq. (1) is

$$\frac{\partial}{\partial t} \rho_s (1 - \phi) c_i^s + \nabla \cdot \rho_s (1 - \phi) \mathbf{V} c_i^s = -\frac{\Gamma c_i^s}{D_i} + \rho_s (1 - \phi) [\lambda_{i-1} c_{i-1}^s - \lambda_i c_i^s] \quad (24)$$

$$\frac{\partial}{\partial t} \rho_f \phi c_i^f + \nabla \cdot \rho_f \phi \mathbf{V} c_i^f = \frac{\Gamma c_i^s}{D_i} + \rho_f \phi [\lambda_{i-1} c_{i-1}^f - \lambda_i c_i^f] \quad (25)$$

The first term on the right hand side of Eqs. (24) and (25) is the change in concentration in the solid and melt due to the production of a melt in local chemical equilibrium with the solid (i.e. an instantaneous fractional melt). The second term is the balance of radioactive production and decay in the solid and liquid respectively. Again, for one-dimensional steady-state melting columns, Eqs. (24) and (25) can be rewritten using Eqs. (20)–(22) to give

$$\frac{dc_i^s}{dz} = \frac{c_i^s (1 - 1/D_i)}{1 - F} \frac{dF}{dz} + \frac{(1 - \phi)}{W_0 (1 - F)} [\lambda_{i-1} c_{i-1}^s - \lambda_i c_i^s] \quad (26)$$

$$\frac{dc_i^f}{dz} = \frac{(c_i^s/D_i - c_i^f)}{F} \frac{dF}{dz} + \frac{\rho_f \phi}{\rho_s W_0 F} [\lambda_{i-1} c_{i-1}^f - \lambda_i c_i^f] \quad (27)$$

Comparing the last term in each of these equations to the equations for  $w$  and  $W$  (Eqs. (21) and (22)) shows that elements travel either at the solid velocity or at the melt velocity but that in either reservoir, the system will tend towards secular equilibrium if unsupported by melting. If  $F(z)$ ,  $D_i(z)$  and  $\phi(z)$  are known functions of height, Eqs. (26)–(27) can be solved numerically for the concentration of all elements in the solid and liquid as a function of height in the column. Note

again that for a stable trace element ( $\lambda_i = \lambda_{i-1} = 0$ ) with constant bulk partition coefficient  $D_i$ , these equations can be solved analytically to show that

$$\frac{c_i^s}{c_{i0}^s} = (1 - F)^{(1/D_i - 1)} \quad (28)$$

$$\frac{c_i^f}{c_{i0}^f} = \frac{1}{F} \int_0^F c_i^s dF = \frac{D_i}{F} \left[ 1 - (1 - F)^{1/D_i} \right] \quad (29)$$

which are precisely the equations for a fractionally melted solid and an aggregated fractional melt.

Equations 13 and 28–29 show that, for stable elements, there is a one-to-one correspondence between the classic equations of batch and fractional melting and the one-dimensional equilibrium melting columns with melt transport. It should be stressed that in either of these calculations, a small porosity or the separation of melts from solid does *a priori* imply that melting is fractional. The important parameter is not the physical melt fraction,  $\phi$ , but the volume of melt that can equilibrate with the solid (in the dynamic melting models, this volume is controlled by  $\phi_{eq}$ ). If the solid re-equilibrates with all of the melt that passes through it, one-dimensional columns will produce small porosity melts with the concentration of a batch melt with degree of melting  $F_{max}$ . If the melt and solid have no interaction during transport, the column produces integrated fractional melts. This result is a rather deep consequence of the strict conservation of mass constraints imposed by the restrictions of one dimensionality and steady-state. In two and three dimensions, additional effects can occur [47, 48].

#### A.4 Approximate solution for the enrichment factor $\alpha_i$

One of the principal properties of the equilibrium transport solution is that it shows two different behaviours depending on whether the extraction time of the daughter element is slow or fast compared to its half-life. To demonstrate that this is the expected behaviour of the governing equations, it is useful to consider an approximate solution to Eq. (15) for the enrichment factor for  $^{230}\text{Th}$ . In the full solution (Figs. 3–5), the effective velocities are a function of height in the column; however, much of the behaviour of the solution can be recovered if we assume that these velocities are approximately constant (but not equal). If we also note that there is little total decay of  $^{238}\text{U}$  during

transport then we can set  $\alpha_U \sim 1$  (Fig. 3c). In this case Eq. (15) can be solved analytically to show that at the top of the column, the enrichment in thorium over batch melting is

$$\alpha_{Th} \sim \left( 1 - \frac{t_U}{t_{Th}} \right) \exp[-\lambda_{Th} t_{Th}] + \frac{t_U}{t_{Th}} \quad (30)$$

where  $t_U = d/\bar{w}_{eff}^U$  and  $t_{Th} = d/\bar{w}_{eff}^{Th}$  are the average extraction times for uranium and thorium respectively, and  $d$  is the depth of the melting column

Therefore, for extraction times that are long compared to the half-life of thorium ( $\lambda_{Th} t_{Th} \gg 1$ ), the enrichment goes to the ratio of the extraction times,  $t_U/t_{Th} = \bar{w}_{eff}^{Th}/\bar{w}_{eff}^U$ . Examination of Eq. (13) shows that this ratio is independent of the upwelling rate  $W_0$ . For long extraction times, it is only the top of the column that controls what can be measured at the surface. Equation (13) shows that, near the top of the column, the ratio of the velocities depends only on porosity and ranges from 1, when there is no melt separation, to a maximum that is the approximately the ratio of the partition coefficients  $D_U/D_{Th}$ . These maximum enrichments occur for large degrees of melting and porosities much smaller than the partition coefficients. This behaviour can be seen in Fig. 5. For short extraction times, Eq. (30) becomes

$$\alpha_{Th} \sim 1 + \lambda_{Th} [t_U - t_{Th}] \quad (31)$$

and depends on the *difference* in extraction time between parent and daughter. The difference in times depends on the upwelling velocity but is independent of  $\phi_{max}$  for porosities much smaller than the partition coefficients. For  $\phi_{max} > D_{Th}$ , the difference in extraction times also depends on porosity and decreases rapidly as the melt separation becomes less significant. Again, this is the behaviour shown in Fig. 5a. The behaviour of  $^{226}\text{Ra}$  is similar to that of  $^{230}\text{Th}$  but the positions of the two behavioural regimes are different because of the differences in half-life and compatibility.